Eur. Phys. J. Special Topics **146**, 249–259 (2007)

DOI: 10.1140/epjst/e2007-00184-9

THE EUROPEAN PHYSICAL JOURNAL SPECIAL TOPICS

Solenoidal spectral formulations for the computation of secondary flows in cylindrical and annular geometries

Solenoidal spectral formulations

A. Meseguer[a], M. Avila[b], F. Mellibovsky[c], and F. Marques[d]

Dept. Applied Physics, Univ. Politecnica de Catalunya, Jordi Girona 1-3, Campus Nord-B5, Barcelona 08034, Spain

Abstract. Novel spectral methods are formulated in terms of divergence-free vector fields in order to compute finite amplitude time-dependent solutions of incompressible viscous flows in cylindrical and/or annular geometries. The numerical discretization of the method leads to a simple dynamical system of amplitudes from which the stability properties of the solution can be analyzed easily. In addition, the formulation allows easy implementation of continuation algorithms to track solutions that have bifurcated from a known state, or the search for disconnected solution branches by means of homotopy transformations of the Navier–Stokes equations. The method is succesfully applied to the study of generic double Hopf bifurcations in pressure-driven helicoidal flows and to the search of unstable travelling wave solutions in pipe flow.

1 Introduction

Spectral methods have been extensively applied to the approximation of solutions of the Navier–Stokes equations [3,6,10]. In particular, pseudospectral methods have become more popular within the computational fluid dynamics community due to their easy implementation and efficiency [13]. By contrast, generalized Petrov–Galerkin methods are far from being competitive in terms of algorithmic performance when compared with fractional step collocation methods because the former need suitable solenoidal vector bases to interpolate and project the approximated solution, thus demanding large memory storage requirements [15,23]. By contrast, splitting collocation methods not only economize the storage of the interpolated solution but also are more adaptable to problems with non-regular boundary conditions. However, the algorithmic structure of a standard fractional step pseudospectral method is less flexible when dynamical features of the problem must be studied. For example, fractional time solvers require taylored methods to compute unsteady solutions using their own time stepper structure to preconditionate the linear system arising from the Newton–Krylov iteration [16]. The spectral computation of flows in axially unbounded cylindrical or annular geometries takes advantage of the periodicity in the axial coordinate so that the spatial discretization leads to a system of decoupled linear operators of smaller dimension. As a result, preconditioning in each Fourier subspace is an easier task.

[a] e-mail: alvar@fa.upc.edu
[b] e-mail: marc@fa.upc.edu
[c] e-mail: fmellibovsky@fa.upc.edu
[d] e-mail: marques@fa.upc.edu

In this work, solenoidal Galerkin formulations capable of simultaneously dealing with several difficulties of the Navier–Stokes equations in axially unbounded cylindrical-annular geometries is presented. First, the construction of solenoidal bases of trial functions for the velocity field in order to satisfy the incompressibility condition identically. In addition, these bases have to satisfy suitable physical boundary conditions at the radial annular boundaries and, in the case of cylindrical domains, also to be analytic in a neighbourhood of the apparent singularity located at the pole so that spectral accuracy is accomplished. Second, the obtention of dual bases of solenoidal test vector fields in order to cancel the pressure terms out in the projection, eventually leading to inner products involving orthogonal or almost-orthogonal functions so the resulting discretized operators are banded matrices. In the case of cylindrical geometry, devising an optimal quadrature rule in the radial variable capable of avoiding clustering of points near the center axis so that time step restrictions become weaker and fast transform are applicable in that coordinate. Third, the implementation of the described discretization within an accurate linearly implicit time marching scheme capable of overcoming the difficulties arising from the stiffness of the resulting systems of ODE. Finally, the whole scheme should be within the core of an efficient continuation scheme, in order to compute unstable flows and, in some cases, to compute other solutions arising from homotopy transformations of the Navier–Stokes equations.

The paper is structured as follows. In section 2 the solenoidal spectral bases are constructed for the annular and cylindrical geometries and a brief outline of the projection method is provided. Section 3 is devoted to the time evolution computations transient flows arising in pipes and also to the accurate computation of steady and time-periodic stable helicoidal flows appearing between concentric cylinders. Finally, section 4 is comprehensively devoted to the formulation of the homotopic continuation scheme within the Petrov–Galerkin formulation and the reliability and performance of the method is applied to the computation of unstable travelling wave solutions in pipe flow.

2 Annular and cylindrical solenoidal bases in axially unbounded domains

Henceforth, two type of domains will be considered. The first one consists of a cylindrical annulus of inner and outer radii r_{i}^* and r_{o}^*, respectively. Although the annulus is unbounded in the axial coordinate, it will be assumed that it has a finite length L^* and periodic boundary conditions in that direction will be imposed later on. By using the *gap*, $d^* = r_o^* - r_i^*$, as the unit of length, the spatial coordinates are rendered dimensionless and the domain is

$$\mathfrak{D}_{\mathrm{a}} = [r_{\mathrm{i}}, r_{\mathrm{o}}] \times [0, 2\pi] \times [0, \Lambda],$$

where $r_{\mathrm{i}} = \eta/(1-\eta)$, $r_{\mathrm{o}} = 1/(1-\eta)$, $\eta = r_{\mathrm{i}}^*/r_{\mathrm{o}}^*$ and $\Lambda = L^*/d^*$. The second one consists of a cylinder of the same length L^* and radius a^*, the last being the unit of length. In this case the domain is:

$$\mathfrak{D}_{\mathrm{c}} = [0, 1] \times [0, 2\pi] \times [0, \Lambda],$$

where $\Lambda = L^*/a^*$. Throughout this work, an arbitrary incompressible flow field $\mathbf{u}$ is approximated by a spectral expansion $\mathbf{u}_{\mathrm{S}}$ of order L in z, order N in θ, and order M in r,

$$\mathbf{u}_{\mathrm{S}}(r, \theta, z, t) = \sum_{l=-L}^{L} \sum_{n=-N}^{N} \sum_{m=0}^{M} a_{lnm}(t)\, \mathbf{\Phi}_{lnm}(r,\, \theta,\, z), \tag{1}$$

where $\mathbf{\Phi}_{lnm}$ are *trial* bases of solenoidal vector fields of the form

$$\mathbf{\Phi}_{lnm}(r,\, \theta,\, z) = \mathrm{e}^{\mathrm{i}(\mathrm{k_o}\, l\, z + n\theta)} \mathbf{v}_{lnm}(r), \tag{2}$$

where $\mathrm{k_o} = 2\pi/\Lambda$ is the fundamental axial mode and where $\mathbf{\Phi}_{lnm}$ satisfies

$$\nabla \cdot \mathbf{\Phi}_{lnm} = 0, \tag{3}$$

for $l = -L, \ldots, L$, $n = -N, \ldots, N$ and $m = 0, \ldots, M$. In general, $\mathbf{u}_{\mathrm{S}}$ will represent a *perturbation* from a known base flow so that the trial bases (2) are periodic in the axial and azimuthal

directions and also cancel at the physical boundaries $r = 1$ of $\mathfrak{D}_{\rm c}$ or $r = r_{\rm i}$, $r_{\rm o}$ of $\mathfrak{D}_{\rm a}$. In addition, the set of functions (2) must be *analytic* at the pole axis of $\mathfrak{D}_{\rm c}$. All the previous requirements are accomplished by choosing a suitable set of quasiorthogonal polynomials in the radial coordinate. The solenoidal condition (3) can be written as [22]

$$\left(\partial_r + \frac{1}{r}\right) u_{lnm} + \frac{{\rm i}n}{r} v_{lnm} + {\rm i}\, l\, {\rm k_o}\, w_{lnm} = 0, \tag{4}$$

with

$$\mathbf{v}_{lnm} = u_{lnm}\, \hat{\mathbf{r}} + v_{lnm}\, \hat{\theta} + w_{lnm}\, \hat{\mathbf{z}} = (u_{lnm}, v_{lnm}, w_{lnm})\,. \tag{5}$$

The Petrov–Galerkin scheme is accomplished when projecting the trial functions above described over a suitable dual or test space of vector fields of the form

$$\mathbf{\Psi}_{lnm} = {\rm e}^{{\rm i}(n\,\theta + {\rm k_o} l\, z)} \tilde{\mathbf{v}}_{lnm}(r). \tag{6}$$

In each geometry, the product $(\mathbf{\Psi},\, \mathbf{\Phi})$ is defined as the volume integral over the domain:

$$(\mathbf{\Psi},\, \mathbf{\Phi})_{\mathfrak{D}_{\rm a,c}} = \int_{\mathfrak{D}_{\rm a,c}} \mathbf{\Psi}^{\dagger} \cdot \mathbf{\Phi}\, {\rm d}\mathfrak{D}_{\rm a,c}, \tag{7}$$

where † stands for complex conjugate transposed, $\mathbf{\Phi}$ belongs to the physical or trial space and $\mathbf{\Psi}$ is a solenoidal vector field belonging to the test or projection space still to be determined. One of the advantages of this product is that it cancels any gradient field, i.e., $(\mathbf{\Psi}, \nabla p) = 0$. In the following two subsections the general framework described above is particularized for the two geometries.

2.1 Annular bases

In what follows, we define:

$$\delta = \frac{1+\eta}{1-\eta}, \qquad x(r) = 2r - \delta, \tag{8}$$

that maps the radial domain $r \in [r_{\rm i}, r_{\rm o}]$ to the interval $x \in [-1, 1]$, and

$$\mathrm{h}_m(r) = (1-x^2)\mathrm{T}_m(x), \qquad \mathrm{g}_m(r) = (1-x^2)^2\mathrm{T}_m(x), \tag{9}$$

where $\mathrm{T}_m(r)$ is the Chebyshev polynomial of degree m, and $\mathrm{w}(x) = (1-x^2)^{-1/2}$ is the weight function within the interval $(-1, 1)$. The functions in (9) satisfy

$$\mathrm{h}_m(r_{\rm i}) = \mathrm{h}_m(r_{\rm o}) = \mathrm{g}_m(r_{\rm i}) = \mathrm{g}_m(r_{\rm o}) = \mathrm{Dg}_m(r_{\rm i}) = \mathrm{Dg}_m(r_{\rm o}) = 0, \tag{10}$$

where D stands for the radial differentiation operator ${\rm d}/{\rm d}r$.

The trial basis for axisymmetric fields ($n = 0$) is given by

$$\mathbf{v}^{(1)}_{l0m}(r) = (0,\, \mathrm{h}_m,\, 0), \qquad \mathbf{v}^{(2)}_{l0m}(r) = (-{\rm i}\, l\, {\rm k_o} r \mathrm{g}_m,\, 0,\, \mathrm{D}[r\mathrm{g}_m] + \mathrm{g}_m), \tag{11}$$

except that the third component of $\mathbf{v}^{(2)}_{l0m}$ is replaced by h_m when $l = 0$, whereas for the non-axisymmetric case the basis is

$$\mathbf{v}^{(1)}_{lnm}(r) = (-{\rm i}\, n\, \mathrm{g}_m,\, \mathrm{D}[r\mathrm{g}_m],\, 0), \quad \mathbf{v}^{(2)}_{lnm}(r) = (0,\, -{\rm i}\, l\, {\rm k_o} r \mathrm{h}_m,\, {\rm i}\, n\, \mathrm{h}_m), \tag{12}$$

except that the third component of $\mathbf{v}^{(2)}_{lnm}$ is replaced by h_m when $l = 0$. For the projection space, the basis corresponding to axisymmetric fields is

$$\tilde{\mathbf{v}}^{(1)}_{l0m}(r) = \mathrm{w}(0,\, r\mathrm{h}_m,\, 0), \qquad \tilde{\mathbf{v}}^{(2)}_{l0m}(r) = r^{-2}\mathrm{w}({\rm i}\, l\, {\rm k_o} \mathrm{g}_m,\, 0,\, \mathrm{D}_+\mathrm{g}_m + 2r^{-1}(1 - x^2 + rx)\mathrm{h}_m), \tag{13}$$

where $\mathrm{D}_+ = \mathrm{D} + r^{-1}$, and the third component of $\tilde{\mathbf{v}}^{(2)}_{l0m}$ is replaced by $r\mathrm{h}_m$ if $l = 0$. The basis for the non-axisymmetric case is

$$\tilde{\mathbf{v}}^{(1)}_{lnm}(r) = \mathrm{w}({\rm i}\, n\, r\mathrm{g}_m,\, r\mathrm{D}_+[r\mathrm{g}_m] + 2xr^2\mathrm{h}_m,\, 0), \quad \tilde{\mathbf{v}}^{(2)}_{lnm}(r) = \mathrm{w}(0,\, {\rm i} l {\rm k_o} r^2 \mathrm{h}_m,\, -{\rm i}\, n\, r\mathrm{h}_m). \tag{14}$$

The projection fields contain the Chebyshev weight function $\mathrm{w}(x)$ so that the resulting radial integratio can be computed exactly by means of quadrature formulas.

2.2 Cylindrical bases

In this case, we define the radial functions

$$\mathrm{h}_m(r) = (1-r^2)\mathrm{T}_{2m}(r), \qquad \mathrm{g}_m(r) = (1-r^2)\mathrm{h}_m(r), \qquad \mathrm{w}(r) = \frac{1}{\sqrt{1-r^2}}, \tag{15}$$

where $\mathrm{T}_{2m}(r)$ is the Chebyshev polynomial of degree $2m$ and $r \in [0,1]$. In this case, the bases must satisfy suitable regularity conditions at the origin [27] and also cancel at $r = 1$,

$$\boldsymbol{\Phi}_{lnm}(1,\, \theta,\, z) = \mathbf{0}. \tag{16}$$

For the axisymmetric trial subspace one possible basis is

$$\mathbf{v}^{(1)}_{l0m} = (0,\, r\mathrm{h}_m,\, 0)\,, \quad \mathbf{v}^{(2)}_{l0m} = (-\mathrm{i}k_o\, l\, r\mathrm{g}_m,\, 0,\, \mathrm{D}_+[r\mathrm{g}_m])\,, \tag{17}$$

except that if $l = 0$, the third component of $\mathbf{v}^{(2)}_{lnm}$ is replaced by $\mathrm{h}_m(r)$. For the non-axisymmetric case the basis is spanned by the elements

$$\mathbf{v}^{(1)}_{lnm} = \left(-\mathrm{i}\, n\, r^{\sigma-1}\, \mathrm{g}_m,\, \mathrm{D}[r^\sigma\, \mathrm{g}_m],\, 0\right), \quad \mathbf{v}^{(2)}_{lnm} = \left(0,\, -\mathrm{i}k_o\, l\, r^{\sigma+1}\, \mathrm{h}_m,\, \mathrm{i}\, n\, r^\sigma \mathrm{h}_m\right), \tag{18}$$

where

$$\sigma = \begin{cases} 2\ (n \text{ even}) \\ 1\ (n \text{ odd}). \end{cases} \tag{19}$$

The binomial factors $(1-r^2)$ and $(1-r^2)^2$ appearing in $\mathrm{h}_m(r)$ and $\mathrm{g}_m(r)$ are responsible for the non-slip boundary conditions (16) at the wall to be satisfied. Factors of the form $1-r$ or $(1-r)^2$ would also solve the boundary problem, but they would violate the parity conditions established by Theorem 1 of [27]. The monomials r, r^σ and $r^{\sigma\pm1}$ appearing in the basis elements enforce regularity and parity conditions at the pole.

The projection basis for the axysimmetric subspace is

$$\tilde{\mathbf{v}}^{(1)}_{l0m}(r) = \mathrm{w}\,(0,\, \mathrm{h}_m,\, 0)\,, \qquad \tilde{\mathbf{v}}^{(2)}_{l0m} = \mathrm{w}\left(-\mathrm{k}_o \mathrm{i}\, l\, r^2 \mathrm{g}_m,\, 0,\, \mathrm{D}_+[r^2\mathrm{g}_m] + r^3\, \mathrm{h}_m\right), \tag{20}$$

except that the third component of the vector in $\tilde{\mathbf{v}}^{(2)}_{l0m}$ is replaced by $r\mathrm{h}_m(r)$ if $l = 0$. For the non-axisymmetric subspace, the projection basis is spanned by the elements

$$\tilde{\mathbf{v}}^{(1)}_{lnm} = \mathrm{w}\left(\mathrm{i}\, n\, r^\beta \mathrm{g}_m, \mathrm{D}[r^{\beta+1}\, \mathrm{g}_m] + r^{\beta+2}\mathrm{h}_m,\, 0\right), \quad \tilde{\mathbf{v}}^{(2)}_{lnm} = \mathrm{w}\left(0,\, -\mathrm{i}k_o l r^{\beta+2}\mathrm{h}_m,\, \mathrm{i}n r^{\beta+1}\mathrm{h}_m\right), \tag{21}$$

except that the third component of the vector in $\tilde{\mathbf{v}}^{(2)}_{lnm}$ is replaced by $r^{1-\beta}\mathrm{h}_m(r)$ if $l = 0$, where

$$\beta = \begin{cases} 0\ (n \text{ even}) \\ 1\ (n \text{ odd}). \end{cases} \tag{22}$$

These vector fields include the Chebyshev factor $(1-r^2)^{-1/2}$ and suitable monomials so that the products between the test and trial functions can be exactly calculated via *Gauss–Lobatto* quadrature, leading to banded matrices.

3 Time evolution

For the stability analysis of a specific steady solution of the Navier–Stokes equation $\mathbf{v}_\mathrm{B}$ we generally track the time evolution of solenoidal disturbances, i.e.,

$$\mathbf{v}(r,\theta,z,t) = \mathbf{v}_\mathrm{B} + \mathbf{u}(r,\theta,z,t), \qquad \nabla\cdot\mathbf{u} = 0. \tag{23}$$

The pressure field would be disturbed accordingly, but its effects will not change the dynamics since gradients cancel out in our projection scheme. On introducing the perturbed fields in the Navier–Stokes equations, we obtain a nonlinear initial-boundary problem for the perturbation $\mathbf{u}$:

$$\partial_t \mathbf{u} = \frac{1}{\mathrm{Re}} \Delta \mathbf{u} - (\mathbf{v}_\mathrm{B} \cdot \nabla)\mathbf{u} - (\mathbf{u} \cdot \nabla)\mathbf{v}_\mathrm{B} - (\mathbf{u} \cdot \nabla)\mathbf{u}, \tag{24}$$

$$\nabla \cdot \mathbf{u} = 0, \tag{25}$$

$$\mathbf{u}(r,\, \theta,\, z,\, 0) = \mathbf{u}_0, \tag{26}$$

for some prescribed initial condition $\mathbf{u}_0$. The Reynolds number appears dividing the laplacian operator when using a space-advective velocity dimensionless system. Using a space-viscous time dimensionless units, the Reynolds number would appear in the linear advective terms, factorizing the basic solution $\mathbf{v}_\mathrm{B}$. By substituting the trial expansion (1) in (24) and projecting over the set of test vector fields,

$$(\boldsymbol{\Psi}_{lnm},\, \partial_t \mathbf{u}_\mathrm{S}) = \left(\boldsymbol{\Psi}_{lnm},\, \frac{1}{\mathrm{Re}} \Delta \mathbf{u} - (\mathbf{v}_\mathrm{B} \cdot \nabla)\mathbf{u} - (\mathbf{u} \cdot \nabla)\mathbf{v}_\mathrm{B} - (\mathbf{u} \cdot \nabla)\mathbf{u} \right), \tag{27}$$

the problem reduces to a dynamical system of amplitudes directly related to the time dependence of the velocity field [6,15,23],

$$\mathbb{A}^{lnm}_{pqr}\ \dot{a}_{pqr} = \mathbb{B}^{lnm}_{pqr}\ a_{pqr} + \mathbb{N}_{lnm}(a), \tag{28}$$

where the convention of sum for repeated subscripts is used. Due to the linearity of the time diferentiation operator ∂_t and the Fourier orthogonality in the periodic variables, the axial and azimuthal modes decouple. The quadratic form $\mathbb{N}_{lnm}(a)$ appearing in (28) corresponds to the projection of the nonlinear convective term that must be calculated via a pseudospectral method. Overall, the resulting stiff system of ODE is integrated in time by means of a linearly implicit Backwards Differentation with explicit polynomial extrapolation for the nonlinear terms.

3.1 Stable secondary flows in annular geometries

We consider an incompressible fluid of kinematic viscosity ν and density ϱ which is contained between two concentric rotating cylinders whose inner and outer radii and angular velocities are r_i^*, r_o^* and Ω_i, Ω_o respectively. In addition, the fluid is driven downstream by an imposed axial pressure gradient. The independent dimensionless parameters appearing in this problem are: the radius ratio $\eta = r_i^*/r_o^*$, which fixes the geometry of the annulus; the Couette flow Reynolds numbers $\mathrm{R_i} = d r_i^* \Omega_i/\nu$ and $\mathrm{R_o} = d r_o^* \Omega_o/\nu$ of the rotating cylinders, where $d = r_o^* - r_i^*$ is the gap between the cylinders, and the axial Reynolds number, $\mathrm{Re} = \bar{w} d/\nu$, where $\bar{w}$ is the mean axial flow velocity in the annulus, and measures the imposed axial pressure gradient. Henceforth, all variables will be rendered dimensionless using d, d^2/ν, and ν^2/d^2 as units for space, time and the reduced pressure ($p = p^*/\varrho$), respectively. The steady velocity field $\mathbf{v}v_B$, independent of the axial and azimuthal coordinates (θ, z), and satisfying $\mathbf{v}_B(r_{\mathrm{i,\,o}}) = \mathrm{R_{i,\,o}}$ is given by the expression

$$\mathbf{v}_B = (u_B,\, v_B,\, w_B) = \big(0,\, C_1 r + C_2/r,\, C_3 \ln(r/r_o) + C_4(r^2 - r_o^2)\big), \tag{29}$$

where

$$C_1 = (\mathrm{R_o} - \eta \mathrm{R_i})/(1+\eta), \tag{30}$$

$$C_2 = \eta(\mathrm{R_i} - \eta \mathrm{R_o})/[(1-\eta)(1-\eta^2)], \tag{31}$$

$$C_3 = 2(1-\eta^2)\mathrm{Re}/(1-\eta^2 + (1+\eta^2)\ln\eta), \tag{32}$$

$$C_4 = (1-\eta)(\ln\eta) C_3/(1+\eta). \tag{33}$$

For Re = 0, i.e., when the basic flow has just azimuthal component, $\mathbf{v}_B$ is called *Circular Couette Flow* (CCF), otherwise it is termed as the *Spiral Poiseuille Flow* (SPF) [12].

In the absence of imposed axial flow, $\mathbf{v}_B$ may exhibit local bifurcations that eventually lead to stable steady secondary regimes. The simplest case that has been comprehensively exemplified in the fluid dynamics literature is the transition from CCF to *Taylor Vortex Flow* (TVF), originally studied by G.I. Taylor in 1923, [31]. The resulting stable flow consists of an array of steady axisymmetric toroidal vortices of selected axial periodicity. The solenoidal Petrov–Galerkin method formulated in section 2.1 has been used to compute this flow. The first stage of the computation consisted of a classical normal mode stability analysis to provide the critical Reynolds number above which the basic flow becomes linearly unstable. This is accomplished by neglecting nonlinear terms of (28) and computing the spectrum of eigenvalues of the linearized operators $\mathbb{L} = \mathbb{A}^{-1}\mathbb{B}$ for a wide range of axial wavenumbers k. This procedure provides the fundamental axial wavenumber $\mathrm{k_o}$ of the secondary stable flow. As a result, the axial periodicity is fixed in the forward integration of (28).

In figure 1(a), the streamfunction corresponding to this solution has been represented on a radial-axial cross section of the cylinder. For the computation of this solution, just $M = 16$ radial modes were required and only $L = 6$ modes were enough to resolve the axial periodicity of the solution. This flow has been computed formerly by many authors in the past as a benchmark of verification of many Navier–Stokes solvers [23]. As long as $\mathrm{R_i}$ is increased further, the TVF solution also becomes unstable and new laminar stable flows appear. These flows are more complex and also time dependent. In this case, a formal modal linearized stability analysis of the TVF is much more complicated. As a result, time integration is the most straightforward tool to identify instability. When increasing the Reynolds number, we monitor the amplitudes of the coefficients a_{lmn} of (28) until exponential growth is observed. The Fourier representation of the flow provides the essential information regarding which axial-azimuthal modes destabilize the flow. After the instability, the time integration will typically converge to a stable limit cycle, originated at the Hopf bifurcation of the TVF.

Figure 1(b) shows a new solution bifurcated from the TVF, usually termed as *Wavy Vortex Flow* (WVF). The Taylor–Couette problem exhibits a broad family of secondary solutions, steady, time periodic, almost time-periodic or even chaotic, that have been repeatedly explored

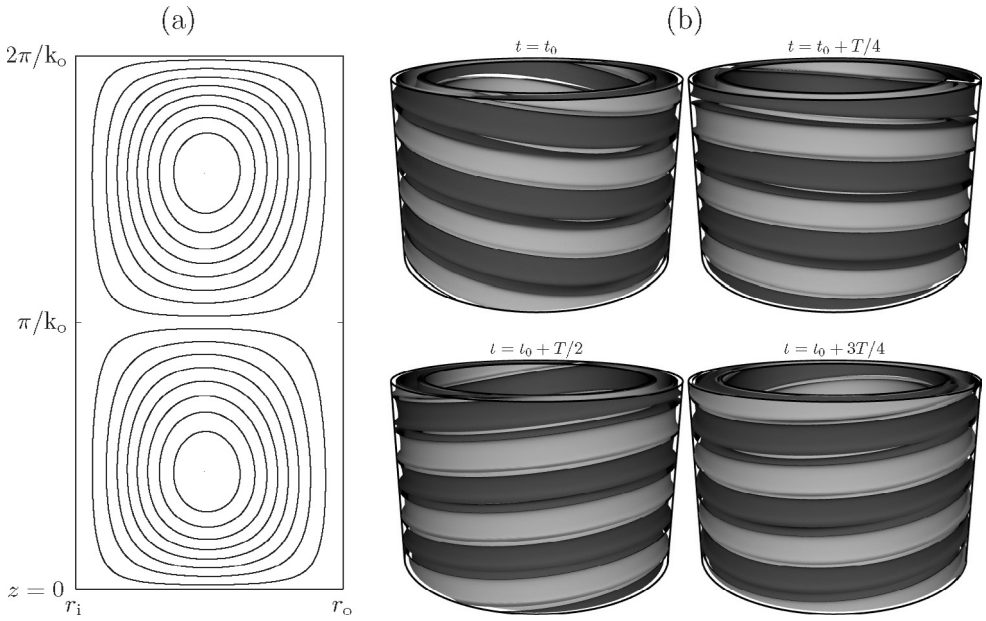

Fig. 1. (a) Streamfunction of a stable TVF solution for $\eta = 0.782$, $\mathrm{R_i} = 105$, $\mathrm{R_o} = 0$, $\mathrm{k_o} = 3.1527$. (b) Snapshots of azimuthal vorticity isosurfaces $(\nabla \times \mathbf{v})_\theta = \pm 30$ corresponding to a stable T-periodic WVF solution for the same value of η and $\mathrm{k_o}$, $\mathrm{R_o} = 0$ and $\mathrm{R_i} = 118$.

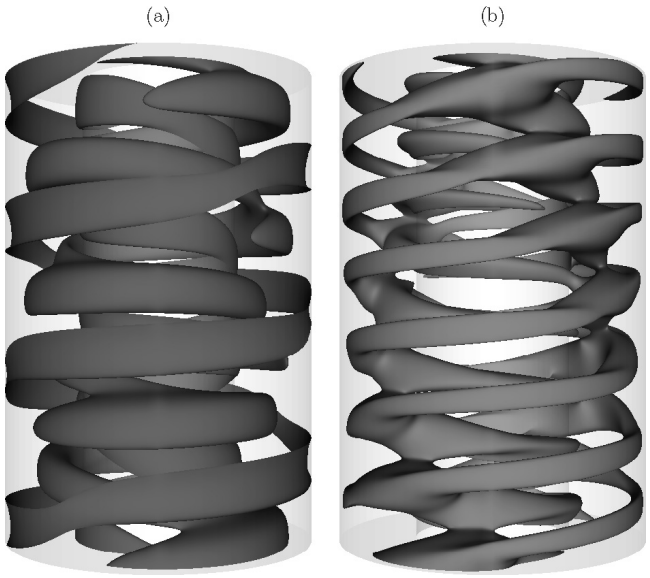

Fig. 2. (a) Azimuthal vorticity isosurface $(\nabla \times \mathbf{v})_\theta = \pm 10$ of a stable IPS solution at $(\mathrm{R_i}, \mathrm{R_o}, \mathrm{Re}) = (201, 414.3, 33)$ and $\eta = 0.5$. (b) *Helicity* isosurface of the corresponding perturbation field, $H = \mathbf{v} \cdot (\nabla \times \mathbf{v}) = 0.2$. In both plots, just one third of the axial domain is shown.

experimentally and computed by many authors in the recent past [1,30]. In all cases explored, perfect agreement with previous simulations and experiments has been obtained.

When the flow is axially driven by an external pressure gradient (SPF), the most common instabilities lead to spiral waves travelling downstream or upstream with selected speeds and angles. In particular, the spectral method has been used to compute secondary regimes consisting of the coexistence of spiral modes of opposite advection speed and angle, formerly observed experimentally by Nagib in the 1970's [12]. When $\mathrm{R_i R_o} > 0$, two or more secondary spiral solutions may bifurcate simultaneously at criticality [2,21]. In a vicinity of the bifurcating point, the features of a *double-Hopf bifurcation* remain and may lead to secondary stable regimes usually termed as *Interpenetrating Spiral Flow* (IPS), consisting of the superposition of spiral solutions of different nature. Figure 2 shows a IPS bifurcated flow from the SPF which contains the main features of the regimes observed by Nagib.

3.2 Intermittency patterns in pipe flow

The Hagen–Poiseuille flow (HPF) is the steady axisymmetric parabolic velocity profile appearing in an infinite pipe of radius a when a fluid of density ρ and kinematic viscosity ν is driven by a uniform axial pressure gradient Π_o [28]. The problem is rendered dimensionless using a and $\mathrm{U_{cl}} = -\Pi_0 a^2/4\rho\nu$ as the units for space and velocity, respectively, where U_cl is the maximum axial speed of the basic HPF profile attained at the *center line* of the pipe. As a result, the basic HPF reads

$$\mathbf{v}_\mathrm{B} = (0,\ 0,\ 1 - r^2), \tag{34}$$

and the Reynolds number is $\mathrm{Re} = a U_\mathrm{cl}/\nu$. The phenomenon of destabilization of this flow has puzzled many fluid dynamicists for over a century and yet there is no clue regarding the inner mechanisms responsible for the transition to turbulence in pipe flows [8,11,28,34,35]. All theoretical and numerical studies suggest that HPF has the peculiarity of being linearly stable for all Reynolds numbers [20,26,27,29], therefore this flow never suffers a local bifurcation. However, this flow becomes turbulent in the experiments for $\mathrm{Re} > 2100$ in a natural fashion [28,34]. In general, HPF instability is characterized by being fast and explosive [8], without traces of selection patterns or transient coherent structures during the transition. However, some

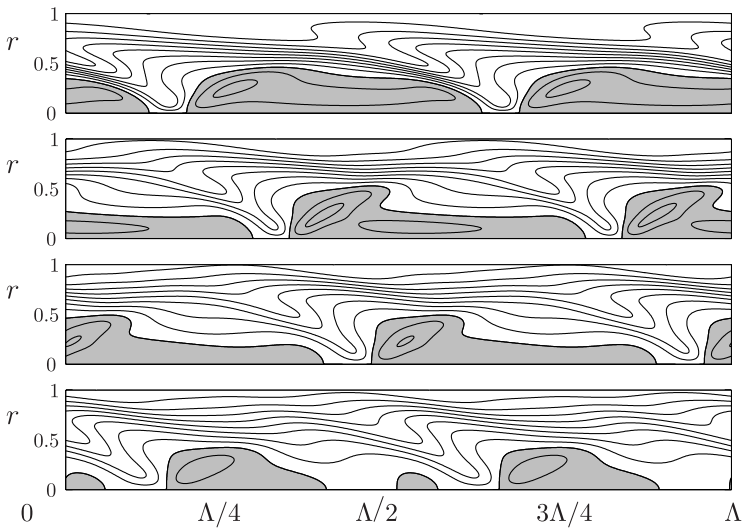

Fig. 3. Equilibrium puff for Re = 2200, following [25], flow from left to right. From top to bottom, the plots show the averaged azimuthal vorticity snapshots at $t = 20, 50, 70, 100$.

experiments carried out in the past [34,35] reported intermittency patterns, usually termed as *puffs* within the range $2100 < \mathrm{Re} < 2200$. The transition in this case is characterized by a robust turbulent spot that preserves its length and the axial speeds of its trailing and leading edges which form the boundary between laminar and turbulent flow. The trailing edge also contains a recirculation bubble of vorticity that makes this structure easily identificable [35].

One of the difficulties of testing the spectral method in the pipe flow is the absence of other stable solutions, apart from the basic HPF. Therefore, the solenoidal spectral formulation has been applied to simulate the aforementioned puffs as well as other transitional regimes [17,19]. To the authors' knowledge, the first numerical simulation of the puffs was provided by O'Sullivan and Breuer [25] using a fractional step collocation method in a constant mass-flux computational pipe. The puff was generated by adding to the basic flow a weakly stable eigenmode suitably scaled up in amplitude. We have reproduced O'Sullivan and Breuer computations by adding to the basic flow an helicoidal initial perturbation of the form

$$\mathbf{u}_{\mathrm{S}}^{0} = \mathbf{u}_{\mathrm{3D}}^{0} = \mathrm{A}\ \boldsymbol{\Phi}_{110}^{(1)} + \mathrm{c.c.}, \tag{35}$$

characterized by being weakly streamwise-dependent and non-axisymmetric. The spatial resolution used to simulate the puff is $(L_z,\, N_\theta,\, M_r) = (128, 32, 32)$ grid points, with aspect ratio $\Lambda = 32\pi$. With this specifications, the perturbation (35) excites the azimuthal-axial pairs $(n, \mathrm{k}) = (\pm 1, \pm 0.06)$. Following O'Sullivan and Breuer [25], the average of the azimuthal vorticity,

$$\langle (\nabla \times \mathbf{v})_\theta \rangle_\theta = \frac{1}{2\pi} \int_0^{2\pi} (\nabla \times \mathbf{v})_\theta \, \mathrm{d}\theta, \tag{36}$$

has been monitored throughout different stages of the transitional dynamics. The results are shown in figure 3, to be compared with figure 8 of [25] and figure 10 of [35]. To help visualization, contours of the averaged vorticity have been plotted on an axial-radial cross section and the regions where this vorticity is negative have been gray coloured to better identify the puff. The L-shaped puff structure near the axis is clearly shown as well as the recirculation bubble at its trailing edge. Overall, the simulation above described required nearly two days on a 3 GHz CPU.

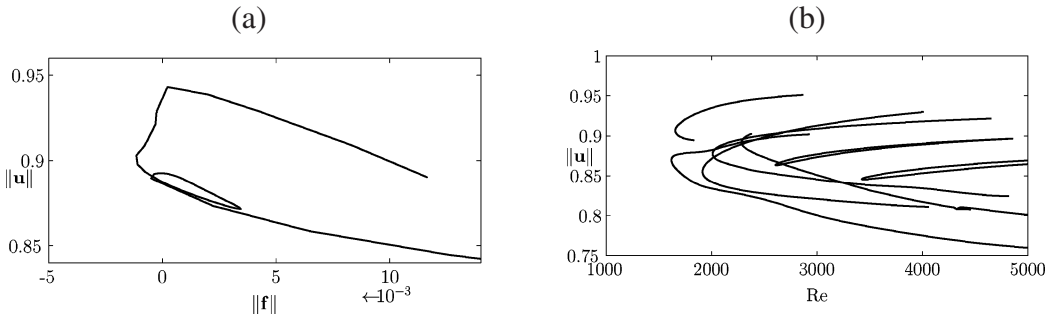

Fig. 4. (a) Amplitude $\|\mathbf{u}\|$ of a C_2-forced TWS as a function of the forcing norm $\|\mathbf{f}\|$. (b) Sadddle nodes of different non-forced TWS of different azimuthal symmetry.

4 Global bifurcations in pipe flow

Since the HPF is linearly stable, its transition can only be explained in terms of global bifurcations. In other words, the topology of the basin of attraction of the basic solution must somehow be affected by the presence of secondary finite amplitude solutions disconnected from the basic regime. Something similar occurs in *Plane Couette Flow* (PCF), i.e., viscous flow between parallel plates relatively sliding with constant speed. As in the pipe problem, PCF has been proved to be linearly stable for all Reynolds numbers, yet it becomes turbulent in practice. Finite amplitude solutions for the PCF were first obtained by Clever and Busse and also by Nagata by introducing centrifugal or thermal forcing in the Navier–Stokes equations so that the resulting problem admitts new solutions [7,24]. By tracking these solutions back with a quasiestatic removal of the forcing, some of this solutions were found to remain in the original PCF. Same attempts were tried for the HPF by Kerswell and Davey and by Barnes and Kerswell without success, by introducing centrifugal terms and for elliptical pipes [4,14].

Waleffe's reformulation of near-wall turbulence theory, originally developed by Benney [5], leads to the identification an energy bootstrapping mechanism within the boundary layer of a shear flow. This mechanism, usually termed as *Self Sustained Process* (SSP) is based on the process by which streamwise vortices substract energy from the basic solution, leading to a modulation of the steady flow that generates streaks or inflectional profiles that become unstable with respect to specific three-dimensional waves [32]. To close the cycle, nonlinear selection rules must regenerate the streamwise vortices again. These ideas were used by Wedin and Kerswell and also by Faisst and Eckhardt in order to find a suitable homotopy transformation in the Navier–Stokes equations so that this cycle could be closed artificially. With this technique, *Travelling Wave Solutions* (TWS) have been recently found in the pipe problem [9,33]. Our next challenge has been to reproduce these new solutions with the solenoidal method.

We proceed to explain how the Petrov–Galerkin scheme is adapted to compute TWS. The first stage consists of adding a suitable homotopy forcing $\mathbf{f}$ to the Navier–Stokes equations so that streamwise vortices capable of stabilize the SSP are formed. Next step is to integrate forward in time the forced system

$$\mathbb{A}\,\dot{a} = \mathbb{B}\,a + \mathbb{N}(a) + \mathbf{f}. \tag{37}$$

Typically, $\mathbf{f}$ consists of an array of pairs of streamwise vortices. The asymptotic behaviour of the solution of (37) will typically converge to a forced TWS advected downstream with constant axial speed. The accuracy of the TWS is improved by searching travelling solutions of the form

$$a = \sum_{l=-L}^{L} \hat{a}_l\, \mathrm{e}^{-\mathrm{i}\,l\,\mathrm{k}\,c\,t}, \tag{38}$$

to equation (37), where c is the axial speed of the wave still to be determined exactly. Introducing the expansion (38) in (37), the solenoidal spectral scheme leads to a decoupled system of nonlinear equations for each axial l-mode,

$$\mathrm{F}_l(\hat{a}, c) = \mathrm{i}\, l\, \mathrm{k}\, c\, \mathbb{A}_l\, \hat{a} + \mathbb{B}_l\, \hat{a} + \mathbf{f}_l + \mathbb{N}_l(\hat{a}) = 0, \tag{39}$$

which are solved with a Newton method. The operators $\mathbb{A}_l$ and $\mathbb{B}_l$ are the closure of $\mathbb{A}$ and $\mathbb{B}$ over the l-Fourier subspace, respectively. For each system, $\mathbb{B}_l$ also decouples for each azimuthal mode, and this property is exploited in order to preconditionate the system with the inverse operator $\mathbb{B}_l^{-1}$. Finally, a pseudo-arclength continuation of the forced solution is performed in the space of parameters $(\mathrm{Re}, \|\mathbf{f}\|)$. In the continuation procedure, the forcing amplitude $\|\mathbf{f}\|$ is progressively decreased until a non-forced TWS is (sometimes) found. This continuation is not trivial and may lead to very complex results and unexpected folds in the solution branch, as shown in figure 4(a) for a $n = 2$-forced solution (C_2) at $\mathrm{Re} = 2200$. Figure 4(b) shows the amplitude of non-forced TWS of different azimuthal symmetry computed with the continuation method. In figure 5, a three-dimensional view of a C_3-TWS has been represented to sketch its internal features. In all cases cases computed, excellent agreement has been found with the earlier works of Faisst and Eckhardt and Wedin and Kerswell [9,33].

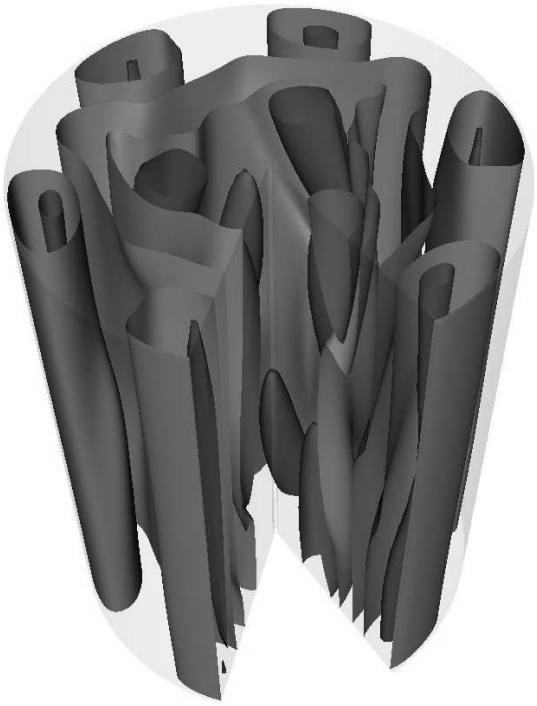

Fig. 5. Three dimensional view of a C_3-TWS.

5 Conclusions

In this work, the computational performance and adaptability of spectral solenoidal schemes to the analysis of local and global stability properties of incompressible flows in cylindrical-annular unbounded domains have been studied. In particular, the developed algorithms are capable of computing steady and time-periodic secondary stable flows in annular geometry via forward time integration. In all cases studied for the Taylor–Couette and spiral Poiseuille flow, the agreement with former experimental and computational works is very good. For cylindrical geometry, the forward time integration reproduces intermittency patterns already observed in pipe flow experiments and the agreement with former DNS simulations is also excellent. Due to the periodicity in the azimuthal and axial coordinate, the formulation of the solenoidal method leads to a modulated data structure that remarkably simplifies the computation and continuation of steady and time-dependent unstable solutions, as well as the homotopy transformations

of the Navier–Stokes equations. This has been exemplified for a really challenging problem as the computation of unstable travelling waves in pipe flow. The presented formulation can also include other effects such as external forcing or stochastic noise. Uncontrolled experimental noise may be relevant when there is a considerable number of clustered secondary solutions. To the authors' experience, the inclusion of noise terms has not been necessary to obtain perfect agreement with the experiments so far. Nevertheless, this and other issues will be addressed in the future.

This work was supported by the Spanish Ministry of Science and Technology, under grants FIS2004-01336 and AP-2004 2235, and by the Catalan Government, grant SGR-00024.

References

1. C.D. Andereck, S.S. Liu, H.L. Swinney, J. Fluid. Mech. **164**, 155 (1986)
2. M. Avila, A. Meseguer, F. Marques, Phys. Fluids **18**, 064101 (2006)
3. J.P. Boyd, *Chebyshev and Fourier Spectral Methods* (Dover, New York, 1999)
4. D.R. Barnes, R.R. Kerswell, J. Fluid. Mech. **417**, 103 (2000)
5. D.J. Benney, R.F. Bergeron, Stud. Appl. Math. **48**, 181 (1969)
6. C. Canuto, M.Y. Hussaini, A. Quarteroni, T.A. Zang, *Spectral Methods in Fluid Dynamics* (Springer-Verlag, Berlin, 1988)
7. R.M. Clever, F.H. Busse, J. Fluid Mech. **344**, 137 (1997)
8. A.G. Darbyshire, T. Mullin, J. Fluid Mech. **289**, 83 (1995)
9. H. Faisst, B. Eckhardt, Phys. Rev. Lett. **91**, 224502 (2003)
10. B. Fornberg, *A Practical Guide for Pseudospectral Methods* (Cambridge University Press, Cambridge, 1996)
11. D. Hof, C.W.H. van Doorne, J. Westerweel, F.T.M. Nieuwstadt, H. Faisst, B. Eckhardt, H. Wedin, R.R. Kerswell, F. Waleffe, Science **305**, 1594 (2004)
12. D.D. Joseph, *Stability of Fluid Motions I and II* (Springer-Verlag, Berlin, 1976)
13. G. Karniadakis, M. Israeli, S.A. Orszag, J. Comput. Phys. **97**, 414 (1991)
14. R.R. Kerswell, A. Davey, J. Fluid Mech. **316**, 307 (1996)
15. A. Leonard, A. Wray, *Proceedings, 8th Int. Conf. on Numerical Methods in Fluid Dynamics,* edited by E. Krause (Springer-Verlag, Berlin, 1982), pp. 335–342
16. C.K. Mamun, L.S. Tuckerman, Phys. Fluids **7**, 80 (1994)
17. F. Mellibovsky, A. Meseguer, Phys. Fluids **18**, 074104 (2006)
18. A. Meseguer, F. Marques, J. Fluid Mech. **455**, 129 (2002)
19. A. Meseguer, F. Mellibovsky, Appl. Num. Math. (2006) (in press)
20. A. Meseguer, L.N. Trefethen, J. Comput. Phys. **186**, 178 (2003)
21. A. Meseguer, F. Marques, Phys. Fluids **17**, 094104 (2005)
22. N. McG. Mhuiris , Appl. Num. Math. **2**, 273 (1986)
23. R.D. Moser, P. Moin, A. Leonard, J. Comput. Phys. **52**, 524 (1983)
24. M. Nagata, J. Fluid Mech. **217**, 519 (1990)
25. P.L. O'Sullivan, K.S. Breuer, Phys. Fluids **6**, 3652 (1994)
26. J. Pretsch, Z. Angew. Math. Mech. **21**, 204 (1941)
27. V.G. Priymak, T. Miyazaki, J. Comput. Phys. **142**, 370 (1998)
28. O. Reynolds, Phil. Trans. R. Soc. Lond. **174**, 935 (1883)
29. H. Salwen, C.E. Grosch, J. Fluid Mech. **54,** 93 (1972)
30. R. Tagg, Nonlinear Sci. Tod. Phys. Fluids **6**, 3652 (1994); **4**, 1 (1994)
31. G.I. Taylor, Phil. Trans. R. Soc. Lond. A **223**, 289 (1923)
32. F. Waleffe, Phys. Fluids **9**, 883 (1997)
33. H. Wedin, R.R. Kerswell, J. Fluid Mech. **508**, 333 (2004)
34. I. Wygnanski, F.H. Champagne, J. Fluid Mech. **59**, 281 (1973)
35. I. Wygnanski, M. Sokolov, D. Friedman, J. Fluid Mech. **69**, 283 (1975)